Journal of Materials Chemistry A

Tailored Nanoscale Interface in Hierarchical Carbon Nanotube Supported MoS2@MoO2-C Electrode toward High Performance Sodium Ion Storage

Journal:	*Journal of Materials Chemistry A*
Manuscript ID	TA-ART-03-2020-003390.R1
Article Type:	Paper
Date Submitted by the Author:	07-May-2020
Complete List of Authors:	Ma, Chunrong; Shandong University Xu, Zhixin; Shanghai Jiao Tong University Jiang, Jiali; Shandong University Ma, Zi-Feng; Institute of Electrochemical and Energy Technology, Chemical Engineering Olsen, Tristan; Boise State University Xiong, Hui; Boise State University, Materials Science and Engineering Wang, Chunguang; Shandong University Yuan, Xian-Zheng; Shandong University, School of Environmental Science and Engineering

Journal Name

ARTICLE

Tailored Nanoscale Interface in Hierarchical Carbon Nanotube Supported MoS_2@MoO_2-C Electrode toward High Performance Sodium Ion Storage

Received 00th January 20xx,
Accepted 00th January 20xx

DOI: 10.1039/x0xx00000x

www.rsc.org/

Chunrong Ma,[a,b] Zhixin Xu,[c] Jiali Jiang,[a] ZiFeng Ma,[c] Tristan Olsen,[b] Hui Xiong,*[,b] Shuguang Wang,*[,a] and Xian-Zheng Yuan*[.a]

Tailoring heterointerfaces at atomic and molecular level in electrode materials for superior structural stability and enhanced power/energy densities is desired yet still challenging for achieving ultrafast and stable Na-ion batteries. Herein, an MoS_2/MoO_2 heterointerface is designed and created, in which ultrafine MoO_2 nanocrystals are tightly anchored on ultrathin MoS_2 nanosheets with the assistance of N-doped carbon protecting layer, on flexible carbon nanotubes. The electrode exhibits high specific capacity of ~700 mAh g^{-1} at 0.2 A g^{-1} and ultra-long cycling stability over 6000 cycles at 5 A g^{-1}. Moreover, excellent rate capability of ~375 mAh g-1 at 10 A g^{-1} is retained. As evidenced by both experiments and density functional theory (DFT) calculations, the heterointerface could not only introduce an electric field to reduce the charge transport barrier, but also provide extra active sites to adsorb Na^+. Meanwhile, within the designed nanoarchitecture, the MoO_2 nanocrystals can effectively reduce the aggregation of MoS_2 during charge/discharge processes, and adsorb polysulfide to improve reversibility. This work provides fundamental understanding of engineering heterointerfaces at atomic level for enhanced Na^+ storage and transport, which can be extended to other functional electrode materials.

Introduction

In the past decades, lithium ion batteries (LIBs) as the energy storage system has been widely applied in the portable electronic products, electric vehicle, and grid-scale energy storage. With the market demand growth, the limited lithium resource and uneven distribution cannot meet the large-scale application.[1-3] Considering the electrochemical similarity between lithium and sodium, sodium ion batteries (SIBs) as one of the most promising candidates aroused extensive attention due to the abundance of the sodium resource in the Earth's crust. However, the ionic radius of Na^+ is larger than that of Li^+, which lead to the sluggish reaction kinetics, severe structure collapse of active material, and unstable solid electrolyte interphase (SEI), these eventually give rise to the inferior electrochemical performance.[4, 5] Therefore, exploring a suitable anode material is the key point to enhance the Na^+ storage for SIBs. Among the anode materials, MoS_2 has been extensively investigated because of the high theoretical specific capacity, and unique two-dimension structure with large interlayer spacing.[6-8] Despite these merits, the application of MoS_2 is still limited by the poor intrinsic conductivity, and structure pulverization with the conversion reaction. Therefore, it is particularly important to rationally design a robust and enhanced structure to promote the reaction kinetic and buffer the volume change simultaneously.

Nanoarchitecturing through robust nano-carbon scaffold has been considered as an effective way to reduce ion diffusion path and relieve volume expansion during cycling.[9-14] Based on such considerations, different MoS_2-carbon composites were explored to improve the cyclability of SIBs, such as MoS_2/graphene, MoS_2/carbon sphere, MoS_2/carbon nanotube, and MoS_2/carbon networks.[15-19] Although progress have been made, challenges still remain for the practical application of MoS_2 in SIBs. Self-aggregation is inevitable during repeat charge/discharge processes because of the weak bonding force between MoS_2 and carbon matrix, leading to the burial of actives sites.[20] Furthermore, the polysulfides generated from the conversion reaction during the discharge process could bring severe redox shuttle issues and lead to irreversible capacity loss.[8] Recently, heterointerface has attracted great attention ranging from optoelectronic devices to electronic instruments, which can afford unprecedented properties by accelerating the charge separation and offering more actives sites. For instance, MoS_2/TiO_2[21] SnS/SnO_2,[22] Sb_2S_3/SnS_2,[23] TiO_2/MoO_2[24] and Co_9S_8/ZnS[25] heterostructures have demonstrated higher specific capacity, enhanced electron mobility and superior rate capability. Nevertheless, the reported heterostructures tend to form dendritic/dumbbell-like morphology owing to the lattice mismatch between different crystal structures, which leads to undesirable structural instability and poor cycling life.

[a]Shandong Key Laboratory of Water Pollution Control and Resource Reuse, School of Environmental Science and Engineering, Shandong University, Qingdao, 266237, China
[b]Micron School of Materials Science and Engineering, Boise State University, Boise, ID 83725, USA
[c]Shanghai Electrochemical Energy Devices Research Centre, School of Chemistry and Chemical Engineering, Shanghai Jiao Tong University, Shanghai, 200240, China

† Footnotes relating to the title and/or authors should appear here.
Electronic Supplementary Information (ESI) available: [details of any supplementary information available should be included here]. See DOI: 10.1039/x0xx00000x

Meanwhile, the interfacial bonding within the heterointerface is crucial to the understanding of the Na^+ storage mechanism in the composites. Thereby, it is urgent to explore new strategies to realize controllable synthesis of stable heterointerfaces and provide more insights regarding the mechanisms of their synergistic effect.

Based on first-principle calculations, nano-heterointerface can effectively improve the structural stability of electrode materials by providing a stronger interface and larger contact area, enabling faster electron transfer.[15] Meanwhile, defects formed between the interfaces could provide an additional pseudocapacitive contribution.[8] Using this as inspiration, we designed a MoS_2/MoO_2 hybrid with an ideal nano-heterointerface, in which few-layer MoS_2 and MoO_2 nanocrystals are sandwiched by N-doped carbon anchoring on carbon nanotube (CNT) surface (CNT-MoS_2@MoO_2-C). This system could provide solutions to the stability challenges associated with MoS_2-based negative electrodes for SIBs. In this structure, MoO_2 nanocrystals are well distributed within MoS_2 nanosheets to avoid the aggregation of MoS_2 during charge/discharge processes, as well as to adsorb polysulfides to improve reversibility. Moreover, the nano-interface between MoS_2 and MoO_2 crystals, compared to traditional limited interfacial contact, could provide additional sites for charge storage and promote electron and ion transport. Furthermore, the N-doped carbon can facilitate fast ion diffusion, and act as the protection shell to strengthen the structural durability of the nanocomposite simultaneously. Consequently, the prepared CNT-MoS_2@MoO_2-C electrode exhibited a high reversible capacity of ~375 mAh g^{-1} at 10 A g^{-1} and excellent cycling stability (stable over 6000 cycles at 5 A g^{-1}). Galvanostatic intermittence titration techniques (GITT) and density-functional theory (DFT) calculations were performed to provide in-depth insights on the interfacial charge storage and transport mechanism. Such synergistic design strategy may open a new avenue for rational design of hierarchical nanostructured electrode materials as well as unveil the role of the interface in hierarchical nanocomposites for high performance SIBs

Results and discussion

The synthesis process of CNT-MoS_2@MoO_2-C is illustrated in Scheme 1. The CNT-MoS_2 composite was first synthesized by a hydrothermal method. Subsequently, the MoO_2 nanocrystals were formed on the MoS_2 nanosheets via self-polymerization of dopamine with $Mo_7O_{24}^{6-}$ under alkaline conditions. Finally, the CNT-MoS_2@MoO_2-C was obtained by thermal treatment under an Ar atmosphere. The morphology and structure features were characterized using scanning electron microscopy (SEM) and transmission electron microscopy (TEM). As shown in Figure 1a, the 1D structure of prepared CNT-MoS_2 is preserved and has a coarse surface, which is uniformly covered by densely packed and wrinkled MoS_2 nanosheets, and the diameter of the prepared CNT-MoS_2 is ~300 nm. Figure 1b shows that the CNT-MoS_2@MoO_2-C maintains the 1D structure after

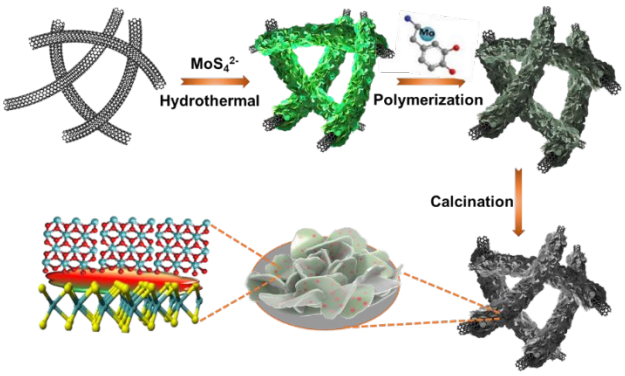

Scheme 1. Schematic illustration of the preparation of CNT-MoS_2@MoO_2-C.

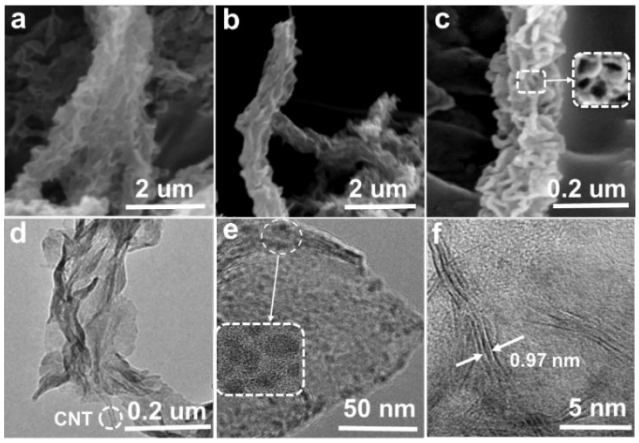

Figure 1. a) SEM image of CNT-MoS_2, b-f) SEM, TEM and high resolution TEM images of CNT-MoS_2@MoO_2-C.

introducing MoO_2 nanocrystals. SEM (Figure 1c) distinctly shows that numerous plate-like structures are vertically aligned on the surface of carbon with a thickness of ~13 nm. From the high-magnification image (Figure 1c inset), voids enclosed by the sheet-structure form at the surface. This porous structure can not only effectively accommodate volume change during repeat charge/discharge processes, but also increase the specific surface area. Figure 1d shows the typical TEM image of CNT-MoS_2@MoO_2-C, where the 1D CNTs are uniformly coated by the 2D structure, indicating the 2D MoS_2 nanosheets with folded structure have been successfully grown on the CNT surface. The TEM image of individual 2D sheets is illustrated in Figure 1e revealing that the MoO_2 nanocrystals are successfully distributed on the surface of MoS_2 sheets without aggregation. To further demonstrate the characteristics of MoO_2 nanocrystals, the high-resolution TEM image (Figure 1e inset) shows the nanocrystals are clearly visible with size of ~3 nm on

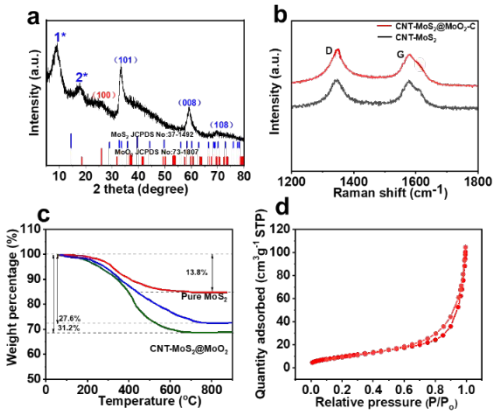

Figure 2. a) XRD pattern of CNT-MoS_2@MoO_2-C, b) Raman profiles of CNT-MoS_2 and CNT-MoS_2@MoO_2-C, c) TGA curves of pure MoS_2 and CNT-MoS_2@MoO_2-C, and d) N_2 adsorption-desorption isotherm of CNT-MoS_2@MoO_2-C.

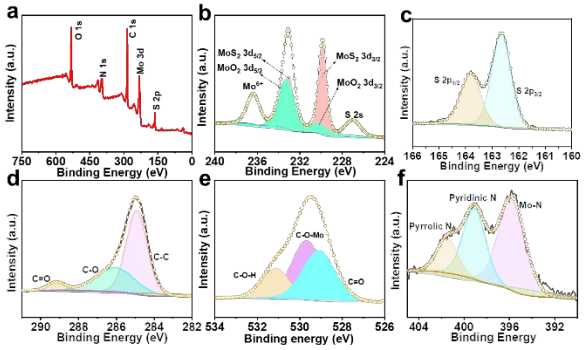

Figure 3. a) All survey, b) the Mo3d, c) S2p, d) C1s, e) O1s, and f) N high-resolutions XPS spectra of CNT-MoS_2@MoO_2-C.

the surface of MoS_2 nanosheet. The well distribution of MoO_2 nanocrystals can be attributed to the polymerization of dopamine together with MoO_4^{2-}. Dopamine contains rich catechol group that have the capability to chelate and adsorb a variety of metal ions during self-polymerization, which would react with the Mo-S group to ensure the MoO_2 crystals can effectively grow on the surface of MoS_2.[26] Meanwhile, the nanocrystals that are uniformly embedded in the carbon matrix form a robust shell, which could reduce aggregation of nanocrystals and restrict nanocrystal growth during the thermal treatment. The few-layered structure with the interlayer distance of 0.96 nm is shown in Figure 1f, which can be ascribed to the (002) lattice plane of MoS_2, indicating the expanded layer feature. To further confirm successfully attachment of MoO_2 nanocrystals on MoS_2 nanosheets, the TEM images of CNT-MoS_2 are detected (as shown in Figure S1 a-b). Bare CNT-MoS_2 obtained from the same experimental procedure without MoO_2-C shows a smooth surface, no nanocrystals can be seen. When MoO_2 nanocrystals introduced on the MoS_2 nanosheets, the surface obviously dotted with well-dispersed nanocrystals (Figure S1 c-d). The MoS_2 and MoO_2 are combined closely under the effect of van der Waal forces near the boundary.[27] In addition, the carbon-induced by the dopamine could strengthen the structural durability of the heterojunction simultaneously.

The structure of the as-prepared CNT-MoS_2@MoO_2-C was further investigated by XRD. In the XRD pattern (Figure 2a), a broad peak can be seen at $2\theta=26.5^o$, which can be attributed to the amorphous MoO_2. All the other diffraction peaks match well with the hexagonal MoS_2 (JCPDS card No. 37-1492). Notably, the (002) peak relating to the crystal structure of multilayer MoS_2 is not detected, but a sharp peak at 8.9^o (1*) and a wide peak at 17.4^o (2*) appear, which can be attributed to the few-layer MoS_2 nanosheets.[15, 18, 28] According to the Bragg's Law ($2d\sin\theta=n\lambda$),[29] the calculated interlayer spacing of peak (1*) is 0.97 nm, which agrees with the TEM results. Raman spectroscopy was carried out to elucidate the crystal structure and composition of the as-prepared nanocomposite. In Figure 2b, there are two distinct peaks located at 1335 and 1574 cm^{-1} for both CNT-MoS_2@MoO_2-C and CNT-MoS_2, representing the D (disorder) and G band (graphitic) of carbon, respectively. Compared to the I_D/I_G of CNT-MoS_2 (0.98), the CNT-MoS_2@MoO_2-C shows a higher I_D/I_G (1.17) due to more defects caused by the N-doped carbon. As shown in Figure S2 the peaks at round 380 and 401 cm^{-1} are detected, which correspond to the in-plane E^1_{2g} mode and out-of-plane A_{1g} mode of MoS_2, respectively.[30] The rest peaks located at 191, 387, 317, and 664 cm^{-1} are the characteristic peaks of MoO_2, demonstrating the successful introduction of MoO_2 on the MoS_2 surface.[31] Thermogravimetric analysis (TGA) was performed to examine the carbon content in the CNT-MoS_2@MoO_2-C composite. According to the literature,[32] MoS_2 can be oxidized to MoO_3 in air, then the pure MoS_2@MoO_2 was also examined for the convenience of quantitative analysis. In comparison with the 13.8% weight loss of pure MoS_2, the CNT-MoS_2 and CNT-MoS_2@MoO_2-C demonstrates 27.6 and 31.2% weight loss, the calculated content of the MoS_2@MoO_2 is 82.6 % (the detail of the calculation is shown in Figure S3). The N_2 adsorption-desorption technique was used to characterize the surface area of the as-prepared sample. A typical IV type isotherm is distinctly observed (Figure 2d). The specific surface area based on Brunauer-Emmett-Teller (BET) measurement is 209 m^2g^{-1}. Such a high specific area could offer more active sites and promote the electron/ion diffusion, leading to the enhanced performance.

To further analyze the composition and chemical state of the as-prepared CNT-MoS_2@MoO_2-C, X-ray photoelectron spectroscopy (XPS) was carried out. In Figure 3a, Mo, S, O, C, and N can be distinctly detected in the XPS survey scan of the sample, indicating the existence of above elements in the CNT-MoS_2@MoO_2-C composite. The high-resolution Mo spectrum is shown in Figure 3b, the two peaks at 229.8 and 233.0 eV with splitting energy of 3.2 eV can be attributed to the $Mo3d_{3/2}$ and $Mo3d_{5/2}$ for MoS_2, respectively.[33] In addition, the other two peaks at the binding energy of 230.3 and 233.3 eV belong to MoO_2 with splitting energy of 3.0 eV.[34] Mo^{6+} was also

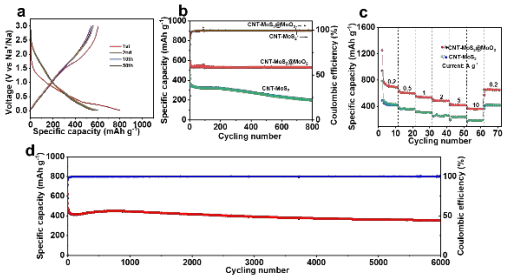

Figure 4. a) Charge-discharge profiles of CNT-MoS_2@MoO_2-C electrode, b) the cycling performance of CNT-MoS_2 and CNT-MoS_2@MoO_2-C electrodes at current 1 A g^{-1}, c) rate capability of CNT-MoS_2 and CNT-MoS_2@MoO_2-C electrodes, and d) long-term cycling performance at current 5 A g^{-1}.

detected at around 236.6 eV, which is associated with the surface oxidation of Mo^{4+} in air.[24] The small peak next to the $Mo3d_{3/2}$ is assigned to the S.[32] To further identified the surface electronic states of as-prepared CNT-MoS_2@MoO_2-C, the Mo bonding states in CNT-MoS_2 and mixture of CNT-MoS_2 and MoO_2-C (CNT-MoS_2/MoO_2-C) are also detected. As shown in Figure S4, the Mo 3d spectrum of CNT-MoS_2 demonstrate typical Mo^{4+}-S peaks at binding energy of 229.3 and 232.5 eV. Compared with the spectrum of CNT-MoS_2, two additional peaks at 229.5 and 233.1 eV can be seen in the spectrum of CNT-MoS_2/MoO_2-C, which can be assigned to the MoO_2 $3d_{3/2}$ and $3d_{5/2}$, suggesting the existence of MoO_2 in the mixture. Note that the Mo^{4+}-S are still located at the same binding energy without shift, which demonstrates the mixture are physically blended without chemical bonds. In comparison, the two peaks of Mo 3d for CNT-MoS_2@MoO_2-Cshifted to higher binding energy values, as a result of the coupling effect of MoS_2 and MoO_2 in the MoS_2/MoO_2 heterostructures.[22, 35] These results agree with the generation of MoS_2/MoO_2 heterostructures as confirmed by XRD and TEM.

From the high-resolution S spectrum (Figure 3c), there are two characteristic peaks at 162.5 and 163.7 eV, which are consistent with the $S2p_{3/2}$ and $S2p_{1/2}$.[36] As shown in Figure 3d, the peaks centered at 284.5, 286.2, and 289.3 eV could be assigned to the C-C, C-O, C=O bonds, respectively.[37] The O 1s peak (Figure 3e) at 529.8 eV can be attributed to the Mo-O signal, which further confirm the existence of MoO_2 in the CNT-MoS_2@MoO_2-C composite. And the other peaks located at 529 and 531.5 eV can be attributed to the C=O and C-OH bond, respectively.[33] The N 1s spectrum is displayed in Figure 3f, an apparent peak at 394.5 eV is corresponding to the Mo-N bond, illustrating N doping and strong interaction in CNT-MoS_2@MoO_2-C. The other peaks at 398.3, and 401.7 eV are ascribed to pyridinic N and pyrrollic N, respectively, which are beneficial for the pseudpcapactive behavior, leading to fast reaction kinetics.[37] The XPS results further prove the formation of as-predicated CNT-MoS_2@MoO_2-C structure.

The electrochemical performance of CNT-MoS_2@MoO_2-C electrode was evaluated in 2032-type coin cells. The galvanostatic charge-discharge profiles of CNT-MoS_2@MoO_2-C at a current of 1A g^{-1} is shown in Figure 4a. The initial discharge and charge specific capacities are 809 and 607 mAh g^{-1}, corresponding to a high Coulombic efficiency of 74% (vs. 56% of the CNT-MoS_2 composite shown in Figure S5). The increased ICE can be attributed to the MoO_2 nanocrystals anchored on 2D nanosheets, which could adsorb the polysulfides to improve the reversibility of MoS_2 at the interface.[38] Meanwhile, the dispersed MoO_2 and N-doped carbon would prevent restacking and agglomeration of MoS_2 during the charge/discharge process, offering more chemical active sites.[34] The initial irreversible capacity loss is mainly associated with the formation of solid electrolyte interphase (SEI) films.[39] From the second cycle, a capacity of 569 mAh g^{-1} can be achieved with an increased Coulombic efficiency of 93%. After 50 cycles, the electrode maintained a highly reversible capacity of 563 mAh g^{-1} and an almost ~100% Coulombic efficiency, which can be attributed to the stable interface. In order to further confirm the superiority of such interface structure, the CNT-MoS_2 control was cycled at a current of 1A g^{-1}. As show in Figure 4b, the CNT-MoS_2 electrode shows continued capacity decay and the capacity decreases to about 180 mAh g^{-1} after 800 cycles, which is mainly resulted from the large volume expansion/contraction and uncontrolled aggregation of the active materials during charge/discharge processes. In contrast, the CNT-MoS_2@MoO_2-C can maintain a much higher discharge capacity of 534 mAh g^{-1} with high cycling stability. The rate capability of the CNT-MoS_2@MoO_2-C electrode with various current rates from 0.2 to 10 A g^{-1} are demonstrated in Figure 4c. The CNT-MoS_2@MoO_2-C electrode demonstrates an impressive rate performance, the average capacity of 702, 598, 486, 453, 412 and 398 mAh g^{-1} were delivered at 0.2, 0.5, 1, 2, 5, and 10 A g^{-1}, respectively. In particular, a capacity of ~700 mAh g^{-1} could still be reached when the current was switched back to 0.2 A g^{-1}, after the deep charge/discharge cycles at a high current of 10 A g^{-1} for 10 cycles, which manifests the reversible and facile Na^+ insertion/extraction. As a comparison, the CNT-MoS_2 electrode exhibits inferior specific capacity, only 127 mAh g^{-1} at the current density of 10 A g^{-1}. Notably, the Na^+ storage of CNT-MoS_2@MoO_2-C electrode is significantly enhanced compared with other reported MoS_2-based and MoO_2-based electrodes.[6, 8, 10, 17, 20, 32, 40] To further confirm the effect of heterointerface in the Na^+ storage, the electrochemical performance of CNT-MoS_2/MoO_2-C (CNT-MoS_2 and MoO_2-C are physically blended by grinding without heterojunction) are also evaluated. As shown in Figure S6a, the CNT-MoS_2/MoO_2-C electrode delivered a specific capacity of 200 mAh g^{-1} at current of 1 A g^{-1} along with the continued capacity decay and the capacity decreased to ~150 mAh g^{-1} after 200 cycles. The rate capability of mixture of CNT-MoS_2 and MoO_2-C are also investigated. From Figure S6b, only capacity of 72 and 46 mAh g^{-1} can be reached at current of 5 and 10 A g^{-1}.

Long-term cycling performance is the key attribute for the application of SIBs. However, the large radius of Na^+ makes

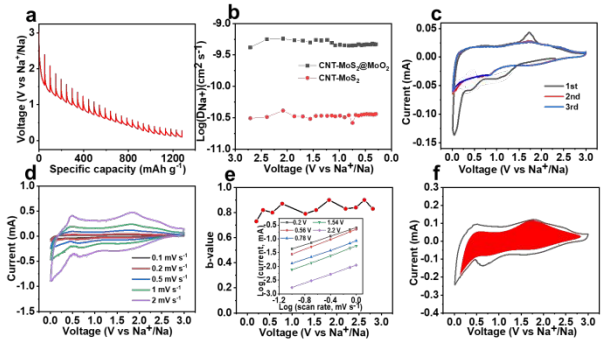

Figure 5. a) GITT profile of CNT-MoS_2@MoO_2-C electrode, b) the corresponding Na^+ diffusion coefficient at different potentials, c) CV curves at scan rate of 0.1 mV s^{-1}, d) CV curves at different scan rate ranging 0.1 to 2 mV s^{-1}, e) the calculated b value at different potentials, and f) the capacitive behavior distinguished form the CV curves at scan rate of 0.5 mV s^{-1}.

the charge transport difficult, and stress associated with volume change inevitably leads to structural collapse. Impressively, the as-prepared CNT-MoS_2@MoO_2-C electrode demonstrates excellent long-term cycling stability (Figure 4d) even at the high current density of 5A g^{-1}. The capacity can be well maintained with ~400 mAh g^{-1} after 5000 cycles with a stable Columbic efficiency of ~100%, which implies the interface structure is highly reversible and stable. The structural stability of the CNT-MoS_2@MoO_2 electrode is evaluated by SEM and TEM after 100 cycles, shown in Figure S7. It can be seen the 1D morphology is well-retained and MoO_2 nanocrystals still uniformly dispersed on MoS_2 nanosheets, which illustrate the highly structural stability.

To elucidate the charge transport mechanisms of Na^+ in CNT-MoS_2@MoO_2-C electrode, the galvanostatic intermittent titration technique (GITT, shown in **Figure S8**) was performed. As shown in **Figure 5a**, the GITT profile of CNT-MoS_2@MoO_2-C was obtained by applying a series of current

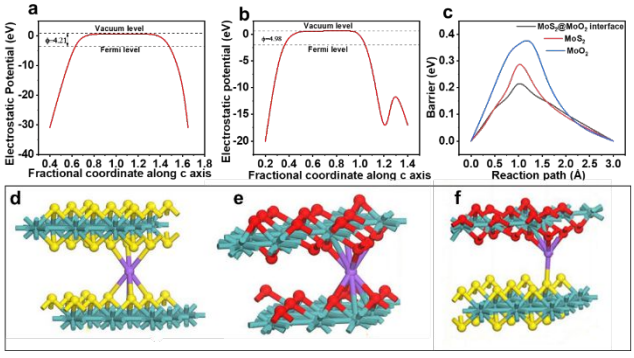

Figure 6. a) MoS_2 and b) MoO_2 electrostatic potentials, c) the diffusion barrier of MoO_2, MoS_2, and MoS_2/MoO_2 interface, and Na adsorption on various system d) MoS_2 interface, e) MoO_2 interface and f) MoS_2/MoO_2 heterointerface.

pulses at 100 mA g^{-1} for 0.5 h followed by a 2 h relaxation process, and the potential change showing in the discharge curve correspond to the Na^+ diffusion rate (D_{Na^+}). According to the equation[41]:

$$D_{Na+} = \frac{4}{\pi}\left(\frac{m_B V_M}{M_B A}\right)^2 \left(\frac{\Delta E_s}{\Delta E_t}\right)^2 \left(\tau \ll \frac{L^2}{D_{Na+}}\right) \quad (1)$$

a series of D_{Na^+} at corresponding potentials can be quantified. The calculated D_{Na^+} of CNT-MoS_2@MoO_2-C is shown in Figure 5b; the diffusivity of Na^+ is mostly constant across the voltage range. Moreover, the D_{Na^+} in CNT-MoS_2@MoO_2-C was higher than that of the CNT-MoS_2 during the whole process, demonstrating enhanced diffusion kinetics by engineering the atomic heterointerface. The atomic heterointerface can effectively restrict the crystal grain growth and offer more crystal defects for fast ion diffusion.[15] Cyclic voltammetry (CV) was conducted to study the charge storage mechanism of CNT-MoS_2@MoO_2-C. Figure 5c reveals the typical CV curves at a scan rate of 0.1 mV s^{-1} within the potential window of 0.01-3V. In the first cycle, a broad reduction peak at 1.0-1.5 V in the cathodic process can be attributed to the intercalation of Na^+ into MoS_2 to form Na_xMoS_2.[42] And the other broad peak at ~0.5 V could be associated with the formation of SEI film and the Na^+ intercalation in MoO_2.[24] The dominant peak at ~0.15 V is assigned to the conversion reaction of Mo and Na_2S.[8] In the following two cycles, the curves overlapped well, illustrating superior reversibility and stability of the CNT-MoS_2@MoO_2-C electrode during the charge/discharge process. Compare with the reported MoS_2-based electrode, CNT-MoS_2@MoO_2-C electrode shows enhanced reversibility, which can be explained to the suppressed shuttle effect by the introduction of MoO_2. To further verify the effect of the MoO_2 nanocrystal in the CNT-MoS_2@MoO_2-C electrode, the CNT-MoS_2@MoO_2-C and CNT-MoS_2 electrodes were disassembled after several cycles at current of 0.1 A g^{-1}. Digital images in Figure S9 clearly shows that the surface of separator and counter electrode in the case of CNT-MoS_2@MoO_2-C was clearly without visible deposition. In contrast, yellow deposits were visible on the surface of the separator for CNT-MoS_2 electrode. These results further demonstrate the effect of MoO_2, which can be combined with polysulfide in atomic heterointerface and then suppresses the shuttle effect.[34] The charge storage mechanism of CNT-MoS_2@MoO_2-C is explored via CV at various scan rates. Figure 5d shows the CV curves at scan rates from 0.1 to 2 mV s^{-1}, which show similar shape. It is assumed that the charge storage

where *a* and *b* are the adjustable parameters, and the *b*-value can be calculated form the slops of log(*v*)–log(*i*) plots. Specifically, the charge storage is controlled by diffusion when *b* is 0.5, whereas b=1 indicates the capacitive behavior dominates the whole process. Figure 5e illustrates a series of *b*-value at different potentials during the cathodic process, and the inset is the plot of log(*v*)–log(*i*). The majority *b* values are higher than 0.8, which suggest the capacitive behavior play a dominant role in the charge storage, promoting fast kinetics. The capacitive contribution to the total charge storage at

mechanism can be studied according to the relationship between the current (i) and scan rate (v)[43]:

$$i = av^b \quad (2)$$

specified scan rate can be quantitatively analyzed according to the following equation:[43]

$$i = k_1v + k_2v^{\frac{1}{2}} \quad (3)$$

where the k_1v represent the capacitive effect, which can be obtained through calculating the k_1. As demonstrated in Figure 5f, the capacitive contribution for the CNT- MoS_2@MoO_2-C electrode at scan rate of 0.5 mV s^{-1} (shaded area) is ~84% of the whole charge storage.

As expected, the CNT-MoS_2@MoO_2-C structure with well-known characteristics have shown the compelling Na^+ storage performance, which mainly benefit from: (1) that the expanded interlayer space can offer more active sites for adsorbing Na^+ and promote fast insertion/extraction of Na^+, resulting in fast reaction kinetics; (2) The shuttle effects of intermediate polysulfides generated through the conversion reaction can be well suppressed by the introduction of MoO_2, which acts as adsorbent to immobilize polysulfides, promoting the reversibility of the reaction. Moreover, the growth of MoO_2 on the MoS_2 surface can avoid the aggregation and restacking of 2D MoS_2 during charge/discharge process, ensuring the exposure the active sites; (3) The CNT and high conductive N-doped carbon as the sandwiched layer can tightly integrate the MoS_2/ MoO_2, which not only increase the charge transfer but also buffer the volume expansion during the charge/discharge process, contributing to the structural stability and cycling reversibility. The electrochemical impedance spectra (EIS) was carried out to better understand the kinetics of the CNT-MoS_2@MoO_2-C, CNT-MoS_2, and MoO_2-C electrodes, the results was fitted by an equivalent electrical circuit (Figure S10). The CNT-MoS_2@MoO_2-C electrode demonstrate a lower charge transfer resistance than the CNT-MoS_2 (869 Ω) and MoO_2-C (567 Ω), which can be attributed to the rapid electron transfer effects of CNT and N-doped carbon in the sandwich-type structure[44]; (4) The enhanced pseudocapacitance with the hierarchical nanostructure can effectively facilitate fast kinetics in charge transfer and transport.

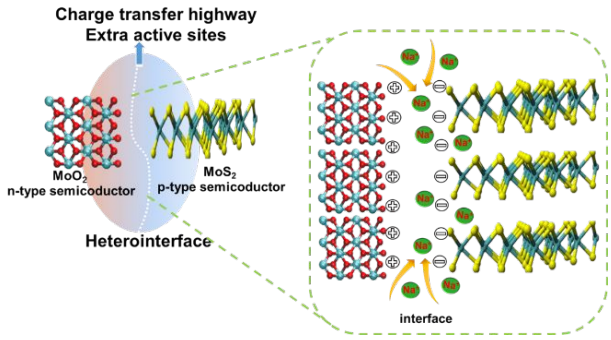

Scheme 2. The summary of the enhanced electrochemical performance of MoS_2/MoS_2 heterointerface.

In addition to the aforementioned merits, the enhancement in capacity of composite electrodes has often been ascribed to the ambiguous "synergetic effect" without further clarification or discussion on the exact roles of interface. In this work, the CNT-MoS_2@MoO_2-C electrode features distinct differences from previous reported composite materials in terms of the nanoscale heterointerface, which could maximize the Na^+ storage and transport. To further understand such interesting atomic heterointerface on the Na^+ storage behavior, DFT calculations were carried out. In this structure, MoS_2 is a typical p-type semiconductor with a band gap of 1.89 eV,[45] while MoO_2 works as a wide band gap n-type semiconductor (3.85 eV).[46] Therefore, the built-in electric field could be present at the heterointerface when the MoS_2/MoO_2 p-n heterojunctions is formed. The electrostatic potentials of the MoS_2 and MoO_2 is examined, respectively, to further reveal the electron distributions in the heterointerface. As shown in Figure 6a and b, MoS_2 demonstrates a lower Fermi level than that of MoO_2. Once the heterointerface is formed, these Fermi levels tend to align. The internal electric field can promote the accumulation of negative charges on the MoS_2 surface and positive charges on the MoO_2 surface, leading to a charge transport pathway from MoO_2 to MoS_2. Under this electric field, Na^+ can strongly adsorbs on the MoS_2 surface due to the electrostatic attraction between Na^+ and the accumulated negative charge. As shown in Figure 6c, the Na^+ diffusion barrier in the MoO_2, MoS_2 and MoS_2/MoO_2 interface were also calculated. From the calculated results, the CNT-MoS_2@MoO_2-C interface demonstrated a lower diffusion barrier (0.24 eV), which is lower than that of MoS_2 (0.33 eV) and MoO_2 (0.41 eV), suggesting that the Na^+ diffusion at the interface is more favorable for faster kinetics. In the LIBs, Jamink and Maier have proposed a "job-sharing" mechanism in which the Li^+ can be stored in the solid/solid interface. This well explains the extra Li storage at the interface. In order to verify if the enhancement of Na^+ storage can be attributed to the interfacial effect in our structure, the Na^+ storage capability of the heterointerface is investigated systematically. According to the calculated results, the Na^+ preferentially adsorbs on the top of the Mo site with the Ead=2.14 eV, which shows stronger binding ability comparing with S (Ead=189 eV). In this configuration, Na^+ lies on the Mo site, and combines with the 3 nearest S atoms in the form of Na-Mo and Na-S bonds, respectively (Figure 6d). Similarly, in the MoO_2 structure, the most stable position is Na^+ adsorption on the Mo site with Ead=1.98 eV. The interface of MoS_2/MoO_2 is engineered by (002) plane of MoS_2 and (100) plane of MoO_2 according to the XRD results. Compared with the singe MoS_2 and MoO_2, the corresponding adsorption energies of. MoS_2/MoO_2 interface demonstrate significant enhancement, giving an Ead=2.89 eV, in which Na aligns with Mo site of MoS_2. The enhancement of the Ead can be reasonably attributed to the synergetic effect of introducing MoO_2 to construct the MoS_2/MoO_2 interface for additional adsorption sites for Na^+. Based on the above calculated results, a reasonable mechanism is proposed to explain the enhancement of the Na^+ storage, as shown in Scheme 2. In our designed interface, the MoS_2 and MoO_2 acts as a p-type and n-type semiconductor, respectively. Therefore, the built-in electric field can be formed when the

heterointerface was constructed, which could accelerate the charge separation and migration efficiencies, promoting fast reaction kinetics. Moreover, the low barrier of interface could reduce the impedance for charge storage further to improve rate capability. Besides providing faster charger-transfer kinetics, the heterointerface could offer extra sites for Na storage.

Conclusions

In summary, In conclusion, we have designed and synthesized a robust 3D nanoarchitecture involving N-doped carbon layer anchoring MoS_2 nanosheets decorated with MoO_2 nanocrystals directly on the CNT surface. The engineered nano-heterointerface between MoS_2 nanosheets and MoO_2 nanocrystal can maximize the interface synergistic effect to reduce the ion transfer barrier, promote faster reaction kinetics, and provide more active sites. Moreover, our nanocomposite with highly conductive CNTs, protecting carbon layers, and uniform distribution of nanocrystals could further promote pseudocapacitive behavior and maintain the stability of the whole composite during the charge/discharge cycles. These characteristics provide a CNT-MoS_2@MoO_2-C electrode with high energy density as well as high cycling stability when used as the negative electrode for SIBs, which are superior to all reported Mo-based negative electrodes in SIBs. Notably, it delivered an excellent rate capacity of 375 mAh g^{-1} at 10 A g^{-1} and ultra-long cycle life over 6000 cycles at 5 A g^{-1}. Based on the insights on atomic heterointerface, the present work could open a new pathway to rational design and fabrication of other hybrid materials for rechargeable batteries.

Acknowledgements

C. Ma and H. Xiong acknowledge support from the National Science Foundation under Grant No. DMR-1454984. This work was also supported by the National Basic Research Program of China (2014CB239700), the National Natural Science Foundation of China (21905160, 21776175), the Natural Science Foundation of Shanghai (19ZR1424600).

Notes and references

1. K. Matsumoto, J. Hwang, S. Kaushik, C.-Y. Chen and R. Hagiwara, *Energy & Environmental Science*, 2019, **12**, 3247-3287.
2. Y. Liu, C. Yang, Q. Zhang and M. Liu, *Energy Storage Materials*, 2019, **22**, 66-95.
3. B. Sun, P. Xiong, U. Maitra, D. Langsdorf, K. Yan, C. Wang, J. Janek, D. Schroeder and G. Wang, *Advanced Materials*, 2019, 10, 1903891.
4. Y. Wang, Y. Wang, Y.-X. Wang, X. Feng, W. Chen, X. Ai, H. Yang and Y. Cao, *Chem*, 2019, **5**, 2547-2570.
5. C. Zhao, L. Liu, Y. Lu, M. Wagemaker, L. Chen and Y.-S. Hu, *Angewandte Chemie-International Edition*, 2019, **58**, 17026-17032.
6. W. Ye, F. Wu, N. Shi, H. Zhou, Q. Chi, W. Chen, S. Du, P. Gao, H. Li and S. Xiong, *Small*, 2019, **10**, 1906607..
7. H. Wu, X. Zhang, Q. Wu, Y. Han, X. Wu, P. Ji, M. Zhou, G. Diao and M. Chen, *Chemical Communications*, 2020, **56**, 141-144.
8. Y. Li, R. Zhang, W. Zhou, X. Wu, H. Zhang and J. Zhang, *Acs Nano*, 2019, **13**, 5533-5540.
9. L. Xing, Q. Yu, B. Jiang, J. Chu, C.-Y. Lao, M. Wang, K. Han, Z. Liu, Y. Bao and W. Wang, *Journal of Materials Chemistry A*, 2019, **7**, 5760-5768.
10. Q. Pan, Q. Zhang, F. Zheng, Y. Liu, Y. Li, X. Ou, X. Xiong, C. Yang and M. Liu, *Acs Nano*, 2018, **12**, 12578-12586.
11. Z. Li, K. Jiang, F. Khan, A. Goswami, J. Liu, A. Passian and T. Thundat, *Science Advances*, 2019, **5,** 2820.
12. S. Lu, T. Zhu, H. Wu, Y. Wang, J. Li, A. Abdelkader, K. Xi, W. Wang, Y. Li, S. Ding, G. Gao and R. V. Kumar, *Nano Energy*, 2019, **59**, 762-772.
13. J. Feng, Y. Dong, Y. Yan, W. Zhao, T. Yang, J. Zheng, Z. Li and M. Wu, *Chemical Engineering Journal*, 2019, **373**, 565-571.
14. Z. Li, Y. Dong, J. Feng, T. Xu, H. Ren, C. Gao, Y. Li, M. Cheng, W. Wu and M. Wu, *Acs Nano*, 2019, **13**, 9227-9236.
15. H. Jiang, D. Ren, H. Wang, Y. Hu, S. Guo, H. Yuan, P. Hu, L. Zhang and C. Li, *Advanced Materials*, 2015, **27**, 3687-3695.
16. Y. N. Ko, S. H. Choi, S. B. Park and Y. C. Kang, *Nanoscale*, 2014, **6**, 10511-10515.
17. W. Ren, H. Zhang, C. Guan and C. Cheng, *Advanced Functional Materials*, 2017, **27**, 1702116.
18. C. Zhao, C. Yu, B. Qiu, S. Zhou, M. Zhang, H. Huang, B. Wang, J. Zhao, X. Sun and J. Qiu, *Advanced Materials*, 2018, **30,** 1702448..
19. J. Duan, G. Qin, L. Min, Y. Yang and C. Wang, *Acs Applied Materials & Interfaces*, 2018, **10**, 38084-38092.
20. K. Ma, H. Jiang, Y. Hu and C. Li, *Advanced Functional Materials*, 2018, **28,** 1804306..
21. Y. Li, H. Wang, L. Wang, R. Wang, B. He, Y. Gong and X. Hu, *Energy Storage Materials*, 2019, **23**, 95-104.
22. Y. Zheng, T. Zhou, C. Zhang, J. Mao, H. Liu and Z. Guo, *Angewandte Chemie-International Edition*, 2016, **55**, 3408-3413.
23. L. Fang, Z. Lan, W. Guan, P. Zhou, N. Bahlawane, W. Sun, Y. Lu, C. Liang, M. Yan and Y. Jiang, *Energy Storage Materials*, 2019, **18**, 107-113.
24. C. Ma, X. Li, C. Deng, Y.-Y. Hu, S. Lee, X.-Z. Liao, Y.-S. He, Z.-F. Ma and H. Xiong, *Acs Nano*, 2019, **13**, 2664-2664.
25. Y.-Q. Wu, H.-X. Yang, Y. Yang, H. Pu, W.-J. Meng, R.-Z. Gao and D.-L. Zhao, *Small*, 2019, **15,** 1903873.
26. Y. Liu, K. Ai and L. Lu, *Chemical Reviews*, 2014, **114**, 5057-5115.
27. E. Xu, Y. Zhang, H. Wang, Z. Zhu, J. Quan, Y. Chang, P. Li, D. Yu and Y. Jiang, *Chemical Engineering Journal*, 2020, **385,** 123839.
28. D. Ren, Y. Hu, H. Jiang, Z. Deng, P. Saha, H. Jiang and C. Li, *Acs Sustainable Chemistry & Engineering*, 2016, **4**, 1148-1153.
29. S. Zhang, B. V. R. Chowdari, Z. Wen, J. Jin and J. Yang, *Acs Nano*, 2015, **9**, 12464-12472.
30. X. Xie, T. Makaryan, M. Zhao, K. L. Van Aken, Y. Gogotsi and G. Wang, *Advanced Energy Materials*, 2016, **6,**

1502161.

31. S. Wang, Z. Zhang, Y. Yang and Z. Tang, *Acs Applied Materials & Interfaces*, 2017, **9**, 23741-23747.
32. Z. Chen, D. Yin and M. Zhang, *Small*, 2018, **14**, 1703818.
33. Y. Liu, Y. Xiao, F. Liu, P. Han and G. Qin, *Journal of Materials Chemistry A*, 2019, **7**, 26818-26828.
34. X. Zhao, H.-E. Wang, Y. Yang, Z. G. Neale, R. C. Masse, J. Cao, W. Cai, J. Sui and G. Cao, *Energy Storage Materials*, 2018, **12**, 241-251.
35. K. Zhu, X. Wang, J. Liu, S. Lo, H. Wang, L. Yang, S. Liu and T. Xie, *Acs Sustainable Chemistry & Engineering*, 2017, **5**, 8025-8034.
36. X.-Y. Yu, H. Hu, Y. Wang, H. Chen and X. W. Lou, *Angewandte Chemie-International Edition*, 2015, **54**, 7395-7398.
37. C. Ma, C. Deng, X. Liao, Y. He, Z. Ma and H. Xiong, *Acs Applied Materials & Interfaces*, 2018, **10**, 36969-36975.
38. R. Li, X. Zhou, H. Shen, M. Yang and C. Li, *Acs Nano*, 2019, **13**, 10049-10061.
39. Z. Zhu, S. Xi, L. Miao, Y. Tang, Y. Zeng, H. Xia, Z. Lv, W. Zhang, X. Ge, H. Zhang, J. Wei, S. Cao, J. Chen, Y. Du and X. Chen, *Advanced Functional Materials*, 2019, **29,** 1904843.
40. B. Chen, H. Lu, J. Zhou, Y. Chao and S. Z. Qiao, *Advanced Energy Materials*, 2018, **26,** 1702909.
41. T.-T. Shan, S. Xin, Y. You, H.-P. Cong, S.-H. Yu and A. Manthiram, *Angewandte Chemie-International Edition*, 2016, **55**, 12783-12788.
42. M. Hou, Y. Qiu, G. Yan, J. Wang, D. Zhan, X. Liu, J. Gao and L. Lai, *Nano Energy*, 2019, **62**, 299-309.
43. J. Wang, J. Polleux, J. Lim and B. Dunn, *Journal of Physical Chemistry C*, 2007, **111**, 14925-14931.
44. N. Zheng, G. Jiang, X. Chen, J. Mao, Y. Zhou and Y. Li, *Journal of Materials Chemistry A*, 2019, **7**, 9305-9315.
45. S. Chuang, C. Battaglia, A. Azcatl, S. McDonnell, J. S. Kang, X. Yin, M. Tosun, R. Kapadia, H. Fang, R. M. Wallace and A. Javey, *Nano Letters*, 2014, **14**, 1337-1342.
46. D. O. Scanlon, G. W. Watson, D. J. Payne, G. R. Atkinson, R. G. Egdell and D. S. L. Law, *The Journal of Physical Chemistry C*, 2010, **114**, 4636-4645.